Inorganic Chemistry

pubs.acs.org/IC

Article

Solid-State Synthesis Enables Enhanced Crystallinity and Tunable Optical Properties in Lanthanum Oxytelluride

Melissa S. Orr, Hoa H. Nguyen, Thomas S. Ie, Muhammad N. Huda, Mercouri G. Kanatzidis, Michael Bozlar, and Robin T. Macaluso*

Cite This: https://doi.org/10.1021/acs.inorgchem.4c04594

Read Online

ACCESS | Metrics & More | Article Recommendations | Supporting Information

ABSTRACT: Elucidating synthetic parameters to produce crystalline solid-state materials with specific properties remains an outstanding obstacle. Oxychalcogenide materials present their own challenges; gaseous reagents are difficult to control and quantify, and reactions cannot be monitored in situ at elevated temperatures. In this paper, we aim to address the lack of fundamental understanding of oxychalcogenides through the synthesis of La_2O_2Te, by two different routes: traditional solid-state and hydrogen gas-assisted methods. We elucidate the two synthetic pathways by X-ray diffraction (XRD) and scanning electron microscopy to demonstrate distinct characteristics between the crystalline and bulk structures, as well as the growth mechanisms of the oxytelluride products. The differences in optical properties at the macroscopic scale correlate with shifts and broadening of the XRD peaks that distinguish two oxytelluride products. The combination of DFT calculations and photoemission yield spectroscopy suggests that oxygen vacancies may explain differences in the optical properties. Finally, this work provides critical synthetic parameters that will enhance the exploratory synthesis of oxychalcogenide materials.

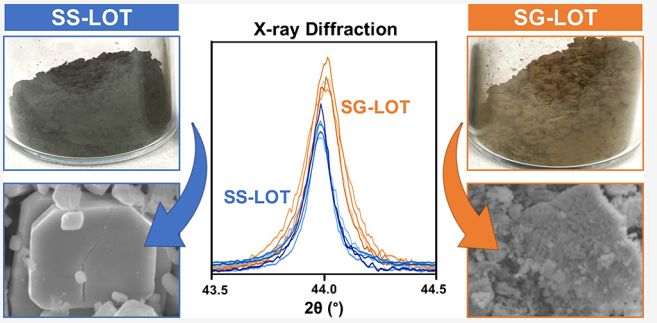

INTRODUCTION

Solid-state materials with interesting magnetic, electronic, and optical properties are cornerstones of many advanced technologies and remain a highly active field of research. These materials have been synthesized by a wide range of techniques from the conventional high-temperature solid-state method to hydrothermal, sol−gel, and vapor transport methods.[1−3] Elucidating reaction mechanisms and predicting the structure and properties of solid-state materials via these techniques are necessary to achieve "synthesis by design"[4,5] of extended inorganic structures. Recent attempts have been made with the use of artificial intelligence to predict materials for specific applications, e.g., permanent magnets, superhard materials, photovoltaics, and thermoelectrics;[6−9] however, these techniques are not yet mature enough to develop synthetic strategies. Hence, exploratory synthesis is still being used to heuristically determine reaction conditions, e.g., reaction environment, thermodynamic conditions (temperature and pressure), and reactants' states of matter, to target solid-state materials with specific physical and chemical properties.[10]

Heteroanionic compounds, which consist of multiple anionic species, possess unique coordination geometries and crystal structures that can give rise to novel materials for various applications, e.g., photocatalysis and thermoelectrics.[11−16] Historically, there have been two common methods employed for the synthesis of oxychalcogenides.[17,18] The first involves a solid−solid route where reactants are heated to temperatures below their melting points, typically under static vacuum, and is sometimes referred to as a ceramic or "shake-n-bake" method. This requires extended dwelling at high temperatures to accommodate the slow diffusion rates of solids and yields the final product in days to weeks. The second method follows a solid−gas route, where a gas (or vapor) reacts with a metal oxide. This time-saving method exploits the fast diffusion rates of gases, yielding the final product within hours, and is most often seen in the hydrogen-assisted sulfurization of metal oxides using H_2S gas.[19] The development of *in situ* characterization techniques has advanced the exploration of solid-state reaction pathways, even at high temperatures and under various environments, and has provided valuable mechanistic insights into the effects of synthesis conditions on reaction pathways and material properties.[20] However, there remains little knowledge of synthesis routes toward oxychalogenides, which boast many

Received: October 27, 2024
Revised: January 24, 2025
Accepted: January 30, 2025

promising clean energy applications.[21,22] These materials can be challenging to synthesize due to differences in reactant volatility and anion polarizability. Furthermore, phase segregation of metal oxides and metal chalcogenides frequently occurs during attempts to prepare oxychalcogenide compounds.[23] The number of known oxytelluride compounds is much smaller than those of oxysulfide and oxyselenide compounds, possibly because the structural determination of these materials is often limited due to the fact that samples are formed as powders.[24,25] Successful syntheses of heteroanionic oxychalcogenides, and especially oxytellurides, should then be investigated for mechanistic insights and to provide property comparisons, thereby motivating this study.

There have been ongoing efforts to examine oxychalcogenide reaction pathways using *in situ* diffraction techniques to guide materials design. This work aims to contribute to the development of oxychalcogenide materials by comparing two different synthesis routes toward the oxytelluride La_2O_2Te and the resulting effects on their physical properties. Herein, we monitor our previously established synthetic routes using *in situ* X-ray diffraction (XRD) to provide insight into reaction progression for the solid−solid synthetic route involving La + TeO_2 under vacuum and for a solid−gas route involving La_2O_3 + Te under hydrogen gas flow. We describe the effects of these synthetic routes on the crystal structure using *ex situ* XRD experiments and demonstrate the dependence of crystallinity on the synthetic technique. Electron microscopy studies reveal the differences in oxytelluride products between the two synthetic pathways and provide critical synthetic conditions that favor crystal formation. Together with density functional theory (DFT) calculations, photoemission yield spectroscopy measurements enable us to understand low energy features observed in diffuse reflectance spectroscopy.

EXPERIMENTAL METHODS

Synthesis. Chemicals were used as purchased: La rod (99.9%, Alfa Aesar), La_2O_3 (99.9%, TCI America), α-TeO_2 (99.99%, Alfa Aesar), and elemental Te (99.9999%, Alfa Aesar). Two synthetic methods were adapted toward the synthesis of oxytelluride La_2O_2Te according to procedures described in detail in our previous work.[26] These two methods are herein referred to as SS-LOT for the solid−solid reaction toward La_2O_2Te and SG-LOT for the solid−gas reaction toward La_2O_2Te, or the hydrogen-assisted route. Four SS-LOT samples and four SG-LOT samples were prepared, for a total of eight samples.

***In Situ* Variable-Temperature Powder X-ray Diffraction (VT-PXRD).** A STOE STADI MP high-resolution diffractometer with Debye−Scherrer geometry and an oven attachment (STOE HT) was used to collect temperature-dependent data. The diffractometer was equipped with an asymmetric curved germanium monochromator and a 1D silicon strip detector. For the solid−solid reaction method: starting materials La and TeO_2 were sieved, mixed in a stoichiometric 2:1 ratio, and packed into 0.7 mm diameter carbon-coated quartz capillaries, which were subsequently flame-sealed under static vacuum. Diffraction data were collected every 50 °C up to 300 °C and then every 10 °C up to 600 °C. For the solid−gas reaction method: starting materials La_2O_3 and elemental Te were sieved and packed into a 0.7 mm diameter carbon-coated quartz capillary, which remained open, and the reagents were separated by quartz wool. Hydrogen gas flowed through the capillary at a rate of 0.5 L/min, and the incident beam was initially centered on La_2O_3. **Warning!** *H_2 gas is considered extremely flammable; therefore, proper ventilation and a hydrogen leak detector should be used.* Diffraction data were collected every 50 °C up to 450 °C and then every 10 °C up to 600 °C. For both methods, data were collected using Ag Kα1 radiation (0.55941 Å) operated at 40 kV and 40 mA. Samples were heated at a rate of 10 °C/min where temperature stability is typically 0.1 °C. Capillaries containing the samples were spun during data collection.

***Ex Situ* Powder X-ray Diffraction (PXRD).** A PANalytical Empyrean diffractometer with Bragg−Brentano geometry was used to collect the room-temperature powder X-ray diffraction data. Data were collected using Ni-filtered Cu Kα radiation (λ = 1.540598 Å) operating at 45 kV and 40 mA over an angular range $10° \leq 2\theta \leq 90°$, at a scan rate of 0.04°/min and step width 0.008°. Rietveld refinement of laboratory diffraction data was performed using the X'Pert Plus software package and a previously established structural model for La_2O_2Te. Global profile refinement parameters included a scale factor, a specimen displacement parameter, and a peak shape function (U, V, W) using the Caglioti equation. A pseudo-Voigt function was used to fit the peak shape. Unit cell parameters, site occupancies, and isotropic displacement parameters were refined. Rietveld refinements for all eight samples (four samples for each synthetic method) can be found in Figure S2.

Scanning Electron Microscopy (SEM). The morphology of the bulk samples was examined using a scanning electron microscope. Images were collected with a Hitachi S-3000N operated at 25 kV.

UV−Vis Diffuse Reflectance Spectroscopy (DRS). UV−Vis−NIR spectra in diffuse reflectance mode were acquired under ambient conditions by using a Cary 5000 UV−vis−NIR double-beam spectrophotometer equipped with a monochromator. To establish a baseline, $BaSO_4$ powder was employed as a nonabsorbing reference material. For data collection, a mixture of the sample powder and $BaSO_4$ was employed. The reflectance data were transformed into absorbance data using the Kubelka−Munk equation, $\alpha/S = (1 - R)^2/2R$, wherein α and S are the absorption and scattering coefficients, respectively, and R denotes reflectance.[27] The band gap of each sample was then determined through extrapolation of the linear region.

Photoemission Yield Spectroscopy (PYS). PYS measurements were conducted in air using an AC-2, Riken Keiki instrument to ascertain the energy level of the valence band maximum relative to a vacuum. Powdered La_2O_2Te was exposed to a tunable monochromatic UV light ranging from 4.2 to 6.2 eV in a dry air environment. The number of photoelectrons generated was quantified at each excitation energy at an increment of 0.10 eV. Photoelectrons are exclusively generated when the photon energy surpasses the semiconductor's ionization energy. The ionization energy was established by identifying the linear onset of the PYS spectra.

Computational Methods. Formation energy, electronic structures, and optical properties of pristine and oxygen vacancies containing La_2O_2Te were calculated using projected augmented wave (PAW) based density functional theory (DFT).[28,29] All calculations and data analysis were performed using the Vienna Ab Initio Simulation Package (VASP) and postprocessing code VASPKIT.[30] The exchange−correlation was approximated by the generalized-gradient approximation (GGA) described by Perdew−Burke−Ernzerhof (PBE) functionals.[31] Plane-wave cutoff energy of 600 eV was used throughout the calculations, affording well-converged results. Monkhorst−Pack k-point sampling was used with 9 × 9 × 3 k-point mesh for the pristine La_2O_2Te unit cell. Oxygen vacancies were introduced to a 3 × 3 × 2 La_2O_2Te supercell with a 3 × 3 × 3 k-point sampling. Due to the layered structure of La_2O_2Te, geometry-dependent van der Waals correction[32,33] was applied for better optimization of crystal structure. The absorption coefficients $\alpha(\omega)$ are calculated by the equation below, where c is the speed of light and $\varepsilon_1(\omega)$ and $\varepsilon_2(\omega)$ are the real and imaginary parts of the dielectric constants:[34]

$$\alpha(\omega) = \frac{\sqrt{2}\,\omega}{c}\left[\sqrt{\varepsilon_1^2(\omega) + \varepsilon_2^2(\omega)} - \varepsilon_1(\omega)\right]^{1/2}$$

RESULTS AND DISCUSSION

Two synthetic methods were adapted toward the synthesis of oxytelluride La_2O_2Te and are herein referred to as SS-LOT for the solid−solid reaction toward La_2O_2Te and SG-LOT for the

https://doi.org/10.1021/acs.inorgchem.4c04594
Inorg. Chem. XXXX, XXX, XXX−XXX

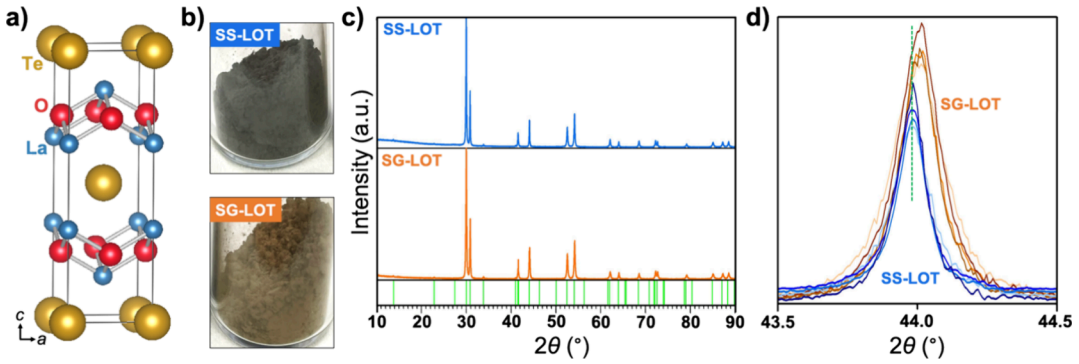

Figure 1. (a) Crystal structure of La_2O_2Te with La (blue), O (red), and Te (yellow). (b) Photos of SS-LOT (top) and SG-LOT (bottom) powder samples. (c) *Ex situ* PXRD for SS-LOT and SG-LOT. Green ticks mark peak positions. (d) Zoomed view of the (200) reflection at $2\theta \approx 44.0°$ for four independent SG-LOT and four SS-LOT samples; the dashed vertical line serves as a visual guide.

solid−gas reaction, or hydrogen-assisted route, similar to our earlier work.[26] Figure 1a,b shows the crystal structure and the powder samples as obtained from the SS-LOT and SG-LOT syntheses, respectively. The photographs highlight differences in optical properties, as the samples clearly differ in color, suggesting structural and physical differences. PXRD patterns (Figure 1c) of SS-LOT and SG-LOT show that they both share the anti-$ThCr_2Si_2$ structure type with $I4/mmm$ space group, $a = b \approx 4.12$ Å and $c \approx 13.1$ Å, similar to previous reports.[35] A zoomed-in view (Figure 1d) of the (200) reflection highlights the differences in peak widths between the two types of samples. The refinement results from multiple *ex situ* PXRD data collected from SS-LOT and SG-LOT syntheses are shown in Figure S2 and Tables S1 and S2. A clear shift in the XRD patterns is consistently observed across multiple scans (Figure 1), confirming that interlayer spacing in SG-LOT is smaller than that in SS-LOT. Also, SG-LOT reflections are consistently broader than the SS-LOT ones, indicating synthesis effects on crystallinity and lattice strain. The average crystallite sizes using Scherrer's equation are 24.47 nm ±2.21 and 15.39 nm ±2.59 for SS-LOT and SG-LOT, respectively. Lattice strain calculated using the Williamson−Hall method is 0.13% for SS-LOT and 0.19% for SG-LOT.[36,37] Williamson−Hall plots and a summary of crystallite size and strain calculations are available in Figure S3 and Table S3.

***In Situ* VT-PXRD for SS-LOT.** The VT-PXRD patterns collected for the SS-LOT formation were collected under a vacuum (Figure 2a, stacked plots in Figure S4). Between room temperature and 375 °C, the XRD patterns reflect the presence of the starting materials, La metal, and TeO_2 powder. Above 375 °C, the diffraction patterns are indexed to SS-LOT. No intermediate phases were observed and the formation temperature of SS-LOT is notably lower than that previously reported.[38] This is a remarkably low reaction temperature, especially when considering that reaction temperatures of metal oxides are typically in the range of 600 to 1200 °C.[39]

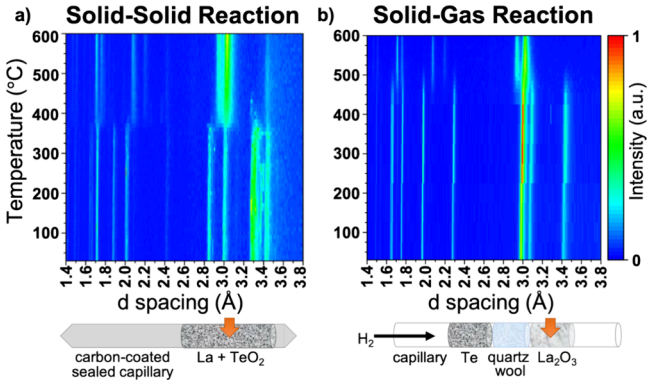

Figure 2. *In situ* VT-PXRD plots and schematic of experimental setup for (a) SS-reaction and (b) SG-reaction. Orange arrows indicate the direction of the incident X-ray beam.

***In Situ* VT-PXRD for SG-LOT.** Figure 2b (and stacked plots in Figure S5) displays the VT-PXRD patterns collected upon heating from room temperature to 600 °C. Only La_2O_3 is observed in the XRD patterns up to 460 °C, at which point, La_2O_3 begins to react and form SG-LOT. Between 460 and 520 °C, diffraction patterns for both La_2O_3 and SG-LOT are observed. Intensities of SG-LOT reflections gradually grow as those for La_2O_3 decrease, with complete phase formation by 520 °C.[40] At 520 °C, all peaks in the diffraction pattern are indexed to SG-LOT, indicating that La_2O_3 is completely consumed. SG-LOT is stable up to 600 °C, the highest temperature that could be reached in our VT-PXRD experiments.

Since the synthesis of SG-LOT involves the use of H_2, we further demonstrate that hydrogen has an important role in the reaction rather than playing the role of a carrier gas as in classic chemical vapor deposition. Indeed, the same reaction under vacuum (instead of hydrogen gas) or N_2 or Ar, does not yield SG-LOT. Also, single crystals of Te metal were found randomly throughout the tube, suggesting that solid tellurium metal simply vaporized upon heating and recrystallized upon cooling (Figure S1). Consequently, we hypothesize that H_2 may contribute to the synthesis of SG-LOT by first reacting with liquid Te metal (Te melts at 449.5 °C).[41] While detecting the active H−Te species is beyond the scope of this work, this can be compared to the common practice of flowing H_2S gas over a metal oxide precursor to synthesize metal oxysulfide compounds, e.g., La_2O_2S,[42] $Ln_2Ti_2S_2O_5$ (Ln = Pr, Nd, Sm, Gd, Tb, Dy, Ho, and Er).[43] Finally, additional studies using gas chromatography coupled with mass spectrometry may help to confirm the role of hydrogen gas in the synthesis.

Scanning Electron Microscopy. To further investigate the growth parameters of La_2O_2Te, SEM studies (Figure 3) were conducted on SS-LOT samples prepared at different dwell temperatures and times. Samples were examined as they were removed from the furnace without any mechanical or chemical handling. Given the large number of variables in the SG-LOT method, we focus on the SS-LOT method and

https://doi.org/10.1021/acs.inorgchem.4c04594
Inorg. Chem. XXXX, XXX, XXX−XXX

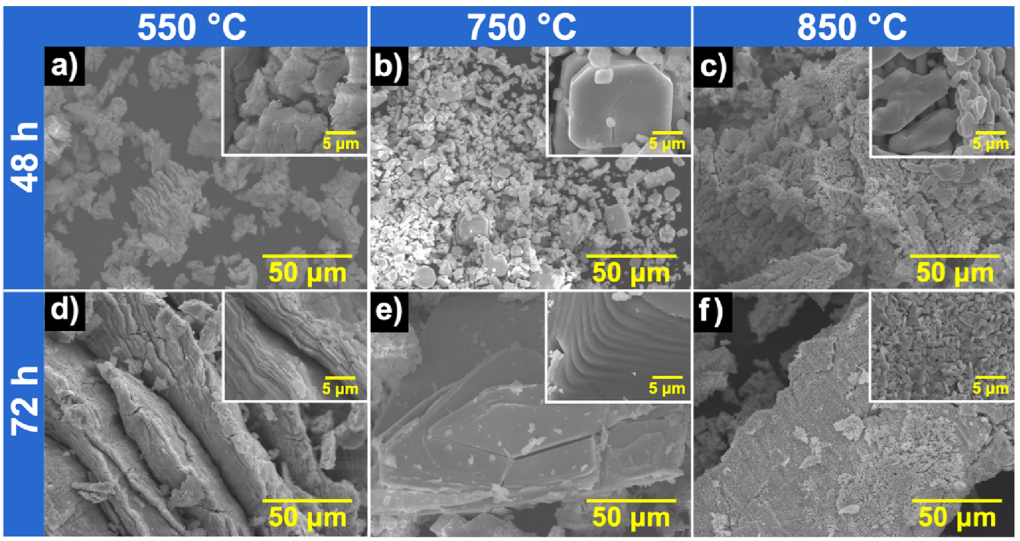

Figure 3. SEM images of SS-LOT samples synthesized at (a) 550, (b) 750, and (c) 850 °C with 48 h dwell times and (d) 550, (e) 750, and (f) 850 °C with 72 h dwell times.

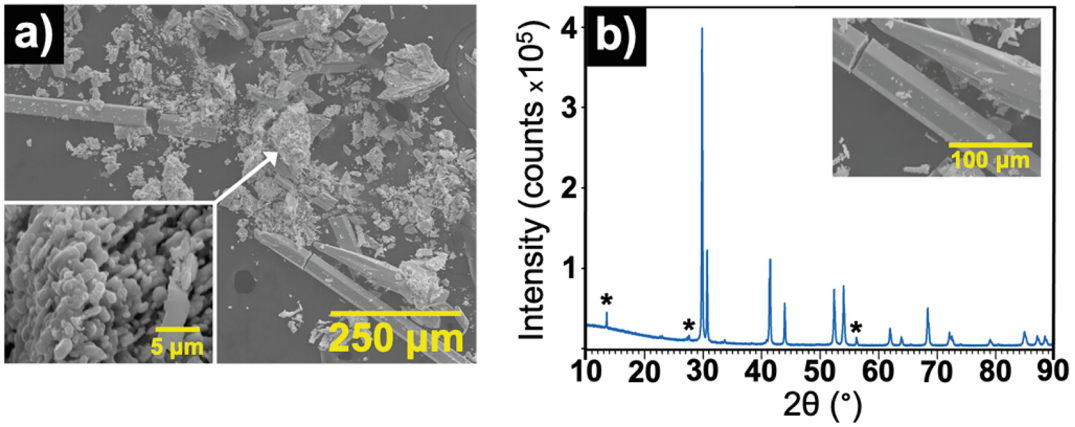

Figure 4. (a) SEM image of $La_2O_2Te_{1-x}$ and Te single crystals produced by solid−solid reaction upon heating to 850 °C with 144 h dwell time. Zoomed-in view of $La_2O_{2-x}Te_{1-y}$ is shown in the inset. (b) PXRD pattern of the same reaction with peaks belonging to $La_2O_{2-x}Te_{1-y}$ and asterisks marking peaks for Te. Inset shows a zoomed-in SEM image of Te single crystals.

compare it with the SG-LOT method (Figure S6) as previously reported. We have previously synthesized SS-LOT at 750 °C;[26] hence, we collected SEM images for samples synthesized below and above this critical temperature, which is just above the melting point of TeO_2 (~733 °C).[40] The samples synthesized at 750 °C for 48 h result in particles with overall sharp edges and smooth surfaces, markers of a crystalline material, with particle sizes reaching 20 μm as a result of the dwelling time (inset, Figure 3b). When the samples were prepared at 850 °C, particles showed signs of coalescence and fusion of primary particles, resulting in overall larger sizes (inset Figure 3c). SEM images for 850 °C for 48 h also tend to indicate a restructuring of the material as evidenced by the loss of crystals present at 750 °C. Samples synthesized at 550 °C for 48 h result in bulk structures that are less crystalline and incompletely formed.

Extending the dwell time from 48 to 72 h at 750 °C produces crystalline particles of up to 200 μm with sharp edges, smooth surfaces, and visible ridges, suggesting a layered growth pattern. An increase in the temperature to 850 °C with a longer dwell time confirms a more pronounced restructuring previously observed after dwelling for 48 h. Similarly, the sample heated at 550 °C for 72 h results in the formation of quasi-layered structures that stem from the 48 h samples.

Given the restructuring of the SS-LOT samples at 850 °C, we further increased the dwell time to 144 h to confirm our observations. Figure 4 shows two products: $La_2O_{2-x}Te_{1-y}$ and Te single crystals. Figure 4 indicates that the native hexagonal needle morphology of Te single crystals is formed using commonly known starting materials La and TeO_2. This result is new and has not been previously reported in the literature. XRD collected on the sample confirmed the presence of Te metal (Figure 4b) along with $La_2O_{2-x}Te_{1-y}$. The stoichiometry of the latter is the result of Te loss at sufficiently long dwell times (exceeding 72 h).

Like the PXRD patterns in Figure 1c, the PXRD pattern in Figure 4b indexes well with the $I4/mmm$ space group, with lattice parameters $a = b = 4.11710(4)$ Å and $c = 13.0811(5)$ Å. However, refinements employing the same structural model with La, Te, and O fully occupying the same atomic positions yielded unreasonably large atomic displacement parameters, B_{iso}, for the Te and the O atoms. Refining occupancies (while restraining B_{iso} to acceptable values) resulted in a visually better fit and a lower R_{wp} (from 9.5 to 8.8%); the occupancies

https://doi.org/10.1021/acs.inorgchem.4c04594
Inorg. Chem. XXXX, XXX, XXX−XXX

refined to values of 1.00, 0.98, and 0.86 for La, Te, and O, respectively. These results corroborate the observation of oxytelluride particles and Te crystals and suggest that extensive dwell times above 72 h result in $La_2O_{2-x}Te_{1-y}$.

Optical and Electronic Properties. Two electronic transitions are observed in the Kubelka–Munk plots for the SS-LOT and SG-LOT samples, as shown in Figure 5a. The lower energy gaps of 0.87 and 0.84 eV are similar in both samples, while the higher energy gaps of 2.86(5) and 2.73(5) eV are observed for SS-LOT and SG-LOT samples, respectively (Table 1). These values are consistently observed among multiple samples, indicating that the optical properties of La_2O_2Te are strongly influenced by the synthetic method.

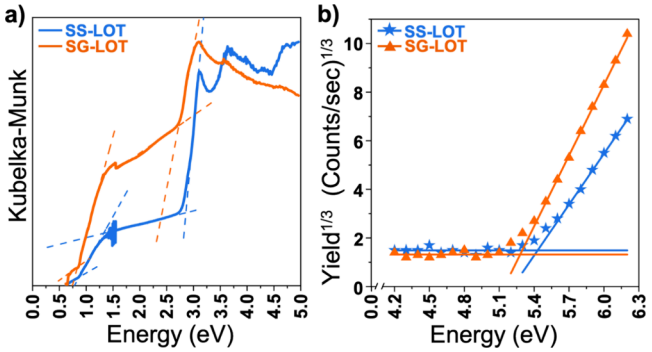

Figure 5. (a) DRS and (b) PYS for SS-LOT (blue) and SG-LOT (orange).

Table 1. Comparative Summary of Average Experimental Results between the Two Synthetic Methods

	SS-LOT	SG-LOT
Reaction onset temperature (°C)	375	460
Strain (%)	0.13(1)	0.19(1)
Crystallite size (nm)	24.47 ± 2.21	15.39 ± 2.59
E_g (eV)	2.86(5)	2.73(5)
E_{VBM} (eV)	5.43(5)	5.28(5)
E_{CBM} (eV)	2.57(7)	2.55(7)

From PYS measurements (Figure 5b), the first ionization energies are determined to be 5.43(5) and 5.28(5) eV for SS-LOT and SG-LOT, respectively. Subtracting the experimentally determined band gap, E_g, from the ionization energy, E_{VBM}, gives the energy level of the conduction band minimum, E_{CBM}, which is determined to be 2.57 and 2.55 eV for SS-LOT and SG-LOT, respectively (Table 1). These results are summarized in Table S4. The difference in E_g values between the SS-LOT and SG-LOT samples is caused by differences in the VBM.

Calculated Electronic Structure and Optical Properties. To better understand the nature of the electronic transitions observed in DRS measurements, the band structure, density of states (DOS), and absorption spectra were calculated. The reliability of our calculations was first established by comparing the experimental and calculated lattice parameters. The crystal structure of pristine La_2O_2Te was relaxed to minimize the interatomic forces and optimize the lattice parameters, and a summary of the results in Table S5 shows less than 1% difference between experimental versus calculated values. Given the propensity of oxygen vacancies in metal oxides and the presence of lattice strain, band structures, DOS plots, and absorption plots were also computed for La_2O_2Te with vacancies. The negative formation energy of oxygen vacancies, shown in Table S6, indicates that such vacancies are thermodynamically favorable when La_2O_2Te is synthesized in environments with little oxygen. SS-LOT and SG-LOT were prepared under a vacuum or in H_2, with little to no oxygen. Therefore, two models—(i) a one-oxygen vacancy model ($La_2O_2Te{:}1V_O$) and (ii) a two-oxygen vacancy model ($La_2O_2Te{:}2V_O$)—were used to compute electronic band structures, DOS, and absorption plots (Figure 6b,c).

Electronic band structure and a DOS plot for pristine La_2O_2Te are shown in Figure 6a. The VBM lies between the N and Γ symmetry points, while the CBM is positioned at the Γ point, resulting in an indirect band gap of 2.06 eV and a direct

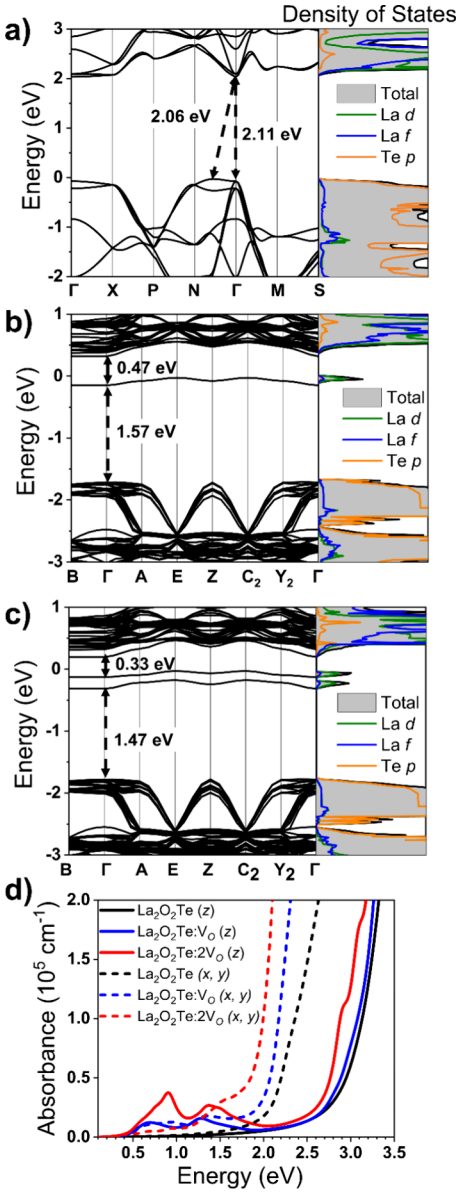

Figure 6. Band structure and density of states plot for (a) pristine La_2O_2Te, (b) $La_2O_2Te{:}1V_O$, and (c) $La_2O_2Te{:}2V_O$, and (d) corresponding calculated optical absorption plots in the *z* direction (solid line) and *x*, *y* direction (dashed line).

https://doi.org/10.1021/acs.inorgchem.4c04594
Inorg. Chem. XXXX, XXX, XXX−XXX

band gap of 2.11 eV (Figure 6a). Although the calculated band gap of La_2O_2Te underestimates our experimental values reported in Table S4, such underestimation of band gaps is a well-known limitation of DFT. While the computed absorption plot for La_2O_2Te (Figure 6d) agrees with the computed band gap for a direct transition (2.11 eV), it does not include the lower energy absorption peak that is observed experimentally (Figure 5a).

Including V_O in electronic structure calculations results in defect La 5d states close to the CBM (Figure 6b,c). A V_O involves the removal of oxygen as a neutral atom, which leads to two electrons being accommodated by empty La 5d orbitals.[44] The gap between the occupied defect La 5d state and the CBM is determined to be 0.47 eV. Introducing a second V_O into the calculation narrows the gap between the defect La 5d state and the CBM (0.33 eV) as well as the gap between the VBM and La 5d states (1.47 eV). Since these gaps are also observed in the computed absorption spectra (Figure 6d), we speculate that these features could be related to the low-energy peaks (below 1.0 eV) in the Kubelka–Munk plots (Figure 5a).

CONCLUSIONS

We demonstrate the strong dependency of the structure and properties of La_2O_2Te on the synthesis parameters using two separate routes. While alternative routes to solid-state synthesis could reduce energy input and time, solid-state synthesis techniques yield oxytelluride products with enhanced crystallinity while hydrogen-assisted synthesis techniques produce samples with oxygen vacancies, potentially affording opportunities to tune optical properties.

The SS-LOT route at 750 °C at 48 h yields La_2O_2Te; however, our SEM and XRD results confirm that this route is sensitive to dwell temperatures and times. As a result, SS-LOT is a method that can be used to produce other oxytelluride products, including nonstoichiometric $La_2O_{2-x}Te_{1-y}$, and Te single crystals with hexagonal morphology. Our results using the SG-LOT route are highly sensitive to the atmosphere, hydrogen being necessary to successfully synthesize La_2O_2Te. Given the complexity of experimental parameters in the SG-LOT route (gas type, flow rate, temperature, etc.), further studies are needed to elucidate the effects of synthesis parameters. Peak widths and shifts in PXRD, combined with DRS and PYSA, reveal that two distinct oxytellurides are formed from each synthetic route. DFT calculations show the potential correlation between electronic structure and optical properties.

ASSOCIATED CONTENT

Supporting Information

The Supporting Information is available free of charge at https://pubs.acs.org/doi/10.1021/acs.inorgchem.4c04594.

Additional experimental details, structural characterization from powder X-ray diffraction, Rietveld refinements, Williamson–Hall plots, and stacked plots of VT-XRD data (PDF)

AUTHOR INFORMATION

Corresponding Author

Robin T. Macaluso − *Department of Chemistry and Biochemistry, University of Texas at Arlington, Arlington, Texas 76019, United States;* orcid.org/0000-0002-0021-0775; Email: robin.macaluso@uta.edu

Authors

Melissa S. Orr − *Department of Chemistry and Biochemistry, University of Texas at Arlington, Arlington, Texas 76019, United States;* orcid.org/0000-0002-3241-5097

Hoa H. Nguyen − *Department of Chemistry and Biochemistry, University of Texas at Arlington, Arlington, Texas 76019, United States;* orcid.org/0000-0002-3375-4998

Thomas S. Ie − *Department of Chemistry, Northwestern University, Evanston, Illinois 60208, United States;* orcid.org/0009-0003-2775-5905

Muhammad N. Huda − *Department of Physics, University of Texas at Arlington, Arlington, Texas 76019, United States;* orcid.org/0000-0002-2655-498X

Mercouri G. Kanatzidis − *Department of Chemistry, Northwestern University, Evanston, Illinois 60208, United States;* orcid.org/0000-0003-2037-4168

Michael Bozlar − *Department of Mechanical & Aerospace Engineering, University of Texas at Arlington, Arlington, Texas 76019, United States;* orcid.org/0000-0002-8320-8557

Complete contact information is available at: https://pubs.acs.org/10.1021/acs.inorgchem.4c04594

Author Contributions

R.T.M. conceived and designed the experiments; M.O. performed synthesis, XRD, and SEM experiments and wrote Experimental Methods and SI sections; H.N. and M.H. performed DFT calculations, H.N. performed SEM experiments; T.I. and M.K. performed PSY experiments. R.T.M. and M.B. wrote the manuscript. All authors have approved the final version of the manuscript.

Notes

The authors declare no competing financial interest.

ACKNOWLEDGMENTS

Work performed at The University of Texas at Arlington was supported by the National Science Foundation Division of Materials Research (NSF DMR 2113689), National Science Foundation (GRFP 2136537), and UTA/NU Partnership for Research and Education in Materials (NSF DMR-2122128). Work performed at Northwestern was supported by the National Science Foundation (DMR-2305731). The computations were performed at the Texas Advanced Computing Center (TACC).

REFERENCES

(1) Schaak, R. E.; Mallouk, T. E. Perovskites by Design: A Toolbox of Solid-State Reactions. *Chem. Mater.* **2002**, *14*, 1455–1471.

(2) Stein, A.; Keller, S. W.; Mallouk, T. E. Turning Down the Heat: Design and Mechanism in Solid State Synthesis. *Science* **1993**, *259* (5101), 1558–1564.

(3) Hodges, J. M.; Xia, Y.; Malliakas, C. D.; Slade, T. J.; Wolverton, C.; Kanatzidis, M. G. Mixed-Valent Copper Chalcogenides: Tuning Structures and Electronic Properties Using Multiple Anions. *Chem. Mater.* **2020**, *32* (23), 10146–10154.

(4) McDermott, M. J.; Dwaraknath, S. S.; Persson, K. A. A Graph-Based Network for Predicting Chemical Reaction Pathways in Solid-State Materials Synthesis. *Nat. Commun.* **2021**, *12* (1), 3097.

(5) Kim, E.; Huang, K.; Saunders, A.; McCallum, A.; Ceder, G.; Olivetti, E. Materials Synthesis Insights from Scientific Literature via

Text Extraction and Machine Learning. *Chem. Mater.* **2017**, *29* (21), 9436−9444.
(6) Kovacs, A.; Fischbacher, J.; Oezelt, H.; Kornell, A.; Ali, Q.; Gusenbauer, M.; Yano, M.; Sakuma, N.; Kinoshita, A.; Shoji, T.; Kato, A.; Hong, Y.; Grenier, S.; Devillers, T.; Dempsey, N. M.; Fukushima, T.; Akai, H.; Kawashima, N.; Miyake, T.; Schrefl, T. Physics-Informed Machine Learning Combining Experiment and Simulation for the Design of Neodymium-Iron-Boron Permanent Magnets with Reduced Critical-Elements Content. *Front. Mater.* **2023**, *9*, 1094055.
(7) Mansouri Tehrani, A.; Oliynyk, A. O.; Parry, M.; Rizvi, Z.; Couper, S.; Lin, F.; Miyagi, L.; Sparks, T. D.; Brgoch, J. Machine Learning Directed Search for Ultraincompressible, Superhard Materials. *J. Am. Chem. Soc.* **2018**, *140* (31), 9844−9853.
(8) Wang, Z.; Yang, M.; Xie, X.; Yu, C.; Jiang, Q.; Huang, M.; Algadi, H.; Guo, Z.; Zhang, H. Applications of Machine Learning in Perovskite Materials. *Adv. Compos. Hybrid Mater.* **2022**, *5*, 2700−2720.
(9) Wang, X.; Sheng, Y.; Ning, J.; Xi, J.; Xi, L.; Qiu, D.; Yang, J.; Ke, X. A Critical Review of Machine Learning Techniques on Thermoelectric Materials. *J. Phys. Chem. Lett.* **2023**, *14* (7), 1808−1822.
(10) Kanatzidis, M. G. Structural Evolution and Phase Homologies for "Design" and Prediction of Solid-State Compounds. *Acc. Chem. Res.* **2005**, *38* (4), 359−368.
(11) Sannes, J. A.; Chatzitakis, A.; Frøen, E. H.; Andersen, N. H. j.; Nilsen, O.; Valldor, M. Characterization and Solid-State UV−Vis Investigations of Photoelectrocatalytically Active $La_5Cl_7[TeO_3]_4$, a Mixed Anion Compound with Alternating 2D Layers of Oxygen and Chlorine. *Inorg. Chem.* **2024**, 18632.
(12) Rahim, W.; Skelton, J. M.; Scanlon, D. O. Ca_4Sb_2O and Ca_4Bi_2O: Two Promising Mixed-Anion Thermoelectrics. *J. Mater. Chem. A* **2021**, *9* (36), 20417−20435.
(13) Kageyama, H.; Hayashi, K.; Maeda, K.; Attfield, J. P.; Hiroi, Z.; Rondinelli, J. M.; Poeppelmeier, K. R. Expanding Frontiers in Materials Chemistry and Physics with Multiple Anions. *Nat. Commun.* **2018**, *9* (1), 772.
(14) Valldor, M. Anion Ordering in Bichalcogenides. *Inorganics* **2016**, *4* (3), 23.
(15) Mishra, V.; Zabolotnii, A.; Mar, A. $La_4Ga_2Se_6O_3$: A Rare-Earth Oxyselenide Built from One-Dimensional Strips. *Inorg. Chem.* **2022**, *61* (31), 12458−12465.
(16) Nakabayashi, M.; Nishiguchi, K.; Liang, X.; Hisatomi, T.; Takata, T.; Tsuchimochi, T.; Shibata, N.; Domen, K.; Ten-no, S. L. Characterization of Planar Defect in Layered Perovskite Photocatalyst $Y_2Ti_2O_5S_2$ by Electron Microscopy and First-Principles Calculations. *J. Phys. Chem. C* **2023**, *127* (16), 7887−7893.
(17) Martinolich, A. J.; Neilson, J. R. Toward Reaction-by-Design: Achieving Kinetic Control of Solid State Chemistry with Metathesis. *Chem. Mater.* **2017**, *29* (2), 479−489.
(18) Clarke, S. J.; Adamson, P.; Herkelrath, S. J. C.; Rutt, O. J.; Parker, D. R.; Pitcher, M. J.; Smura, C. F. Structures, Physical Properties, and Chemistry of Layered Oxychalcogenides and Oxypnictides. *Inorg. Chem.* **2008**, *47* (19), 8473−8486.
(19) Larquet, C.; Carenco, S. Metal Oxysulfides: From Bulk Compounds to Nanomaterials. *Front. Chem.* **2020**, *8*, 179.
(20) Shoemaker, D. P.; Hu, Y. J.; Chung, D. Y.; Halder, G. J.; Chupas, P. J.; Soderholm, L.; Mitchell, J. F.; Kanatzidis, M. G. *In Situ* Studies of a Platform for Metastable Inorganic Crystal Growth and Materials Discovery. *Proc. Natl. Acad. Sci. U.S.A.* **2014**, *111* (30), 10922−10927.
(21) Maeda, K.; Takeiri, F.; Kobayashi, G.; Matsuishi, S.; Ogino, H.; Ida, S.; Mori, T.; Uchimoto, Y.; Tanabe, S.; Hasegawa, T.; Imanaka, N.; Kageyama, H. Recent Progress on Mixed-Anion Materials for Energy Applications. *Bull. Chem. Soc. Jpn.* **2022**, *95* (1), 26−37.
(22) Dey, T.; Mumbaraddi, D.; Wen, F.; Mishra, V.; Michaelis, V. K.; Mar, A. Are Selenides the Same as Sulfides? Structure, Spectroscopy, and Properties of Narrow-Gap Rare-Earth Semiconductors $RE_2Sn(S_{1-x}Se_x)_5$ (RE = La, Ce; x = 0−0.8). *Inorg. Chem.* **2024**, *63* (23), 10726−10736.
(23) Mishra, V.; Mumbaraddi, D.; Iyer, A. K.; Yin, W.; Mar, A. Semiconducting Sm_3GaSe_5O with trigonal bipyramidal $GaSe_5$ units. *J. Solid State Chem.* **2022**, *308*, No. 122901.
(24) Orr, M.; Hebberd, G. R.; McCabe, E. E.; Macaluso, R. T. Structural Diversity of Rare-Earth Oxychalcogenides. *ACS Omega* **2022**, *7* (10), 8209−8218.
(25) Charles, N.; Saballos, R. J.; Rondinelli, J. M. Structural Diversity from Anion Order in Heteroanionic Materials. *Chem. Mater.* **2018**, *30* (10), 3528−3537.
(26) Orr, M. S.; Cruz, K. R.; Nguyen, H. H.; Kojima, A. L.; Macaluso, R. T. Versatility of Tellurium in Heteroanionic Ln_2O_2Te (Ln = La, Ce, Pr) and Tellurate Ln_2TeO_6 (Ln = La, Pr). *Inorg. Chem.* **2022**, *61* (45), 18002−18009.
(27) Murphy, A. Band-gap Determination from Diffuse Reflectance Measurements of Semiconductor Films, and Application to Photoelectrochemical Water-Splitting. *Sol. Energy Mater. Sol. Cells* **2007**, *91* (14), 1326−1337.
(28) Hohenberg, P.; Kohn, W. Inhomogeneous Electron Gas. *Phys. Rev.* **1964**, *136* (3B), B864−B871.
(29) Kohn, W.; Sham, L. J. Self-Consistent Equations Including Exchange and Correlation Effects. *Phys. Rev.* **1965**, *140* (4A), A1133−A1138.
(30) Wang, V.; Xu, N.; Liu, J.-C.; Tang, G.; Geng, W.-T. VASPKIT: A User-friendly Interface Facilitating High-throughput Computing and Analysis Using VASP Code. *Comput. Phys. Commun.* **2021**, *267*, No. 108033.
(31) Perdew, J. P.; Burke, K.; Ernzerhof, M. Generalized Gradient Approximation Made Simple. *Phys. Rev. Lett.* **1996**, *77* (18), 3865−3868.
(32) Grimme, S.; Ehrlich, S.; Goerigk, L. Effect of the Damping Function in Dispersion Corrected Density Functional Theory. *J. Comput. Chem.* **2011**, *32* (7), 1456−1465.
(33) Grimme, S.; Antony, J.; Ehrlich, S.; Krieg, H. A Consistent and Accurate ab initio Parametrization of Density Functional Dispersion Correction (DFT-D) for the 94 Elements H-Pu. *J. Chem. Phys.* **2010**, *132* (15), No. 154104.
(34) Saha, S.; Sinha, T. P.; Mookerjee, A. Electronic Structure, Chemical Bonding, and Optical Properties of Paraelectric $BaTiO_3$. *Phys. Rev. B* **2000**, *62* (13), 8828−8834.
(35) Weber, F. A.; Schleid, T. On Oxytellurides (M_2O_2Te) of the Early Lanthanides (M = La-Nd, Sm-Ho) with anti-$ThCr_2Si_2$-Type Crystal Structure. *Zeitschrift für anorganische und allgemeine Chemie* **1999**, *625* (11), 1833−1838.
(36) Suryanarayana, C.; Norton, M. G. *X-rays and Diffraction*; Springer, 1998.
(37) Cullity, B. D. *Elements of X-Ray Diffraction*; Addison-Wesley Publishing, 1956.
(38) Kent, R. A.; Eick, H. A. The Preparation and Properties of Some Lanthanum(III) Monotelluroöxides. *Inorg. Chem.* **1962**, *1* (4), 956−958.
(39) Block, T.; Schmücker, M. Metal Oxides for Thermochemical Energy Storage: A Comparison of Several Metal Oxide Systems. *Sol. Energy* **2016**, *126*, 195−207.
(40) Haynes, W. M., Ed. *CRC Handbook of Chemistry and Physics*. 95th ed. CRC Press/Taylor and Francis: Boca Raton, 2014.
(41) Kujawa, R. V. Darstellung von Tellur hoher Reinheit. *Physica Status Solidi (b)* **1963**, *3* (6), 1089−1097.
(42) Andreev, P. O.; Sal'nikova, E. I.; Kovenskii, I. M. Preparation of Ln_2O_2S (Ln = Gd, Dy, Y, Er, Lu) in Flowing Hydrogen and Hydrogen Sulfide. *Inorg. Mater.* **2014**, *50* (10), 1018−1023.
(43) Ishikawa, A.; Takata, T.; Matsumura, T.; Kondo, J. N.; Hara, M.; Kobayashi, H.; Domen, K. Oxysulfides $Ln_2Ti_2S_2O_5$ as Stable Photocatalysts for Water Oxidation and Reduction under Visible-Light Irradiation. *J. Phys. Chem. B* **2004**, *108* (8), 2637−2642.
(44) Wang, Z.; Lin, R.; Huo, Y.; Li, H.; Wang, L. Formation, Detection, and Function of Oxygen Vacancy in Metal Oxides for Solar Energy Conversion. *Adv. Funct. Mater.* **2021**, *32* (7), 2109503.

https://doi.org/10.1021/acs.inorgchem.4c04594
Inorg. Chem. XXXX, XXX, XXX−XXX